Journal of Power Sources 576 (2023) 233203

Contents lists available at ScienceDirect

Journal of Power Sources

journal homepage: www.elsevier.com/locate/jpowsour

# Distribution of relaxation times analysis of electrochemical hydrogen pump impedance spectra

Michael Braig [a], Roswitha Zeis [a,b,*]

[a] Karlsruhe Institute of Technology, Helmholtz Institute Ulm, Helmholtzstraße 11, 89081, Ulm, Germany
[b] University of Toronto, Department of Mechanical and Industrial Engineering, 27 King's College Cir, Toronto, ON, M5S, Canada

## HIGHLIGHTS

- Impedance study of a polybenzimidazole-based electrochemical hydrogen pump.
- Selecting the appropriate distribution of relaxation times regularization parameter.
- Identification of proton transfer, kinetics, and mass transport in the impedance.
- Quantification of resistance changes at different operating conditions.

## GRAPHICAL ABSTRACT

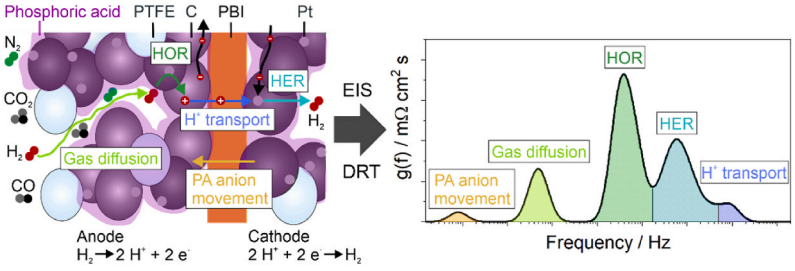


## ARTICLE INFO

*Keywords:*
Electrochemical hydrogen pumping
Polybenzimidazole (PBI)
Electrochemical impedance spectroscopy (EIS)
Distribution of relaxation times (DRT)
Hydrogen oxidation reaction (HOR)
Hydrogen evolution reaction (HER)

## ABSTRACT

Polybenzimidazole-based electrochemical hydrogen pumps (EHPs) allow hydrogen separation from gas mixtures at low cell overpotential. An operating temperature of up to 180 °C provides robustness towards catalyst poisoning by common impurities in steam reformate, like CO or sulfur compounds. Electrochemical impedance spectroscopy (EIS) coupled with the distribution of relaxation times (DRT) analysis is performed on single-cell EHPs supplied by $H_2$ contaminated with $N_2$, $CO_2$, and CO to investigate and quantify the underlying physicochemical processes. By systematically varying the operating parameters, five different processes were identified in the DRT spectrum: the proton transport in the electrode, the hydrogen evolution reaction (HER), the hydrogen oxidation reaction (HOR), the mass transport (MT) in the anode gas diffusion electrode, and the movement of phosphoric acid anions from the cathode to the anode at high current densities. At high contaminant concentrations, the HOR and the MT resistances increase. The HOR inhibition is dominant for CO, while for $N_2$ and $CO_2$, the MT resistance increase is more pronounced. At 180 °C cell temperature, the performance with 50% $CO_2$ in the gas feed was worse than with 1% CO, highlighting the possibility of operating an EHP with a CO-contaminated gas feed at elevated operating temperature.

## 1. Introduction

Currently, $H_2$ is mainly produced via steam reforming of methane. This process generates a mixture of hydrogen and CO, the so-called syngas. Afterward, the syngas is converted into a mixture of $H_2$, $CO_2$, and a small amount of CO in a water-gas-shift reactor. The $H_2$ is subsequently utilized for ammonia production, as a reducing agent in metal production, or fuel cells (FCs). However, further purification is often

* Corresponding author. Karlsruhe Institute of Technology, Helmholtz Institute Ulm, Helmholtzstraße 11, 89081, Ulm, Germany.
*E-mail address:* roswitha.zeis@kit.edu (R. Zeis).

https://doi.org/10.1016/j.jpowsour.2023.233203
Received 23 March 2023; Received in revised form 3 May 2023; Accepted 13 May 2023
Available online 25 May 2023

mandatory since most applications require a higher hydrogen purity than the generated gas [1]. Hydrogen separation methods utilize pressure swing adsorption (PSA), palladium, or polymer membranes. While PSA is the state-of-the-art purification technique for large-scale industrial $H_2$ processing of steam reformate, its power consumption is high, and a high hydrogen purity and gas recovery cannot be achieved simultaneously [2,3]. Palladium membranes currently exhibit the most promising characteristics regarding membrane technologies. However, significant drawbacks include an operating temperature above 350 °C and a maximum pressure difference across the membrane of only 2 bar [4].

Electrochemical hydrogen pumps (EHPs) based on polymer electrolyte membranes (PEMs) allow the simultaneous purification and pressurization of $H_2$ to 1000 bar with a Nafion membrane [5]. However, the temperature operation window of Nafion is limited to approximately 100 °C since liquid water is needed in the gas feed to achieve good proton conductivity. In this temperature range, CO strongly adsorbs onto the platinum catalyst, thus severely decreasing the performance [6]. The hydrogen isolation with Nafion-based EHPs from reformate [7], ethylene [8], $H_2S$, and $CH_4$ [9], and the influence of the operating temperature and the relative humidity (RH) [10] were already investigated previously. The efficiency was relatively low under CO or $H_2S$ contamination, although periodic pulsing on the anode [7] or adding $O_2$ and $O_3$ to the gas feed [9] significantly improved the performance.

EHPs based on a polybenzimidazole (PBI) membrane doped with phosphoric acid (PA) typically operate between 160 and 180 °C. CO desorption is thermodynamically favored at this elevated temperature, considerably decreasing the polarization losses during operation with CO-containing gas [11–13]. Therefore, PBI-based EHPs are suitable for continuous separation of $H_2$ even from heavily contaminated gas mixes. High-temperature EHPs with a PBI membrane and Pt/C catalyst exhibit an excellent CO tolerance, primarily when operated above 160 °C [11–13]. Ion-pair membranes demonstrated stable performance at 200 °C for 100 h and short-term operation at up to 220 °C [14].

Potential application fields for EHPs, besides hydrogen compression and the separation from reformate, are the recycling of hydrogen from the exhaust gas of metal refinement or the extraction from chemical reactors, in which $H_2$ is an unwanted byproduct. Furthermore, EHPs enable the distribution of $H_2$ via the currently existing natural gas network. At the point of use, $H_2$ can be extracted from the natural gas/hydrogen mix by EHPs, and high-purity $H_2$ could be provided in one purification step, e.g., for refueling stations of fuel cell vehicles.

EHPs are commonly characterized by polarization curves (PCs), which permit a simple and fast characterization over the entire performance range [11–15]. However, identifying the underlying processes and their behavior at different operating parameters is not possible with this method. Electrochemical impedance spectroscopy (EIS) quantifies different resistances occurring on different time scales in an electrochemical system. However, assigning features in an impedance spectrum to physicochemical processes is challenging, especially if the frequency ranges of several processes overlap. Physically meaningful interpretations of EIS results are facilitated by the distribution of relaxation times (DRT), which provides an assumption-free impedance spectrum analysis [16–19]. DRT was previously applied successfully to conventional [20] and high-temperature PEM FCs [21–25], SOFCs [26–28], lithium-ion batteries [29,30], and vanadium redox-flow batteries [31,32].

EIS results of high-temperature PEM EHPs are limited [33,34] or were performed only to identify the membrane resistance [35]. Therefore, this paper presents a detailed EIS and DRT characterization of single-cell EHPs with a PA-doped PBI membrane and Pt/C electrodes over various operating parameters. The EHPs were supplied $H_2$ plus different concentrations of $N_2$, $CO_2$, or CO, and operated at varying current density, $H_2$ stoichiometry, temperature, and RH. Five processes could be identified and assigned to physicochemical phenomena, and their resistance changes were correlated to the different operating conditions. The investigation of these processes supports EHP cell development since bottlenecks can be identified and resolved.

## 2. Experimental

### 2.1. Membrane electrode assembly fabrication

Three single cells with an active area of 4 $cm^2$ were assembled with a PBI membrane (Dapozol M40, Danish Power Systems, Denmark) and in-house fabricated gas diffusion electrodes (GDEs). The membranes for all cells were pre-doped in 85% PA (AnalaR Normapur, VWR Chemicals) and had a doping level of 7 g PA per gram PBI. The catalyst layer (CL) was spray-coated onto the microporous layer (MPL) of a commercial gas diffusion layer (GDL, H23C2, Freudenberg, Germany). The ink was prepared by dispersing Pt/C catalyst (20 wt% platinum nanoparticles on carbon black (Alfa Aesar, USA)) and 60 wt% polytetrafluorethylene (PTFE) in water (Dyneon, 3 M, USA) in a 1:1 mixture of water and isopropanol. A tip sonicator was utilized to homogenize the ink for 30 s. Subsequently, the ink was sprayed onto the GDL, which was placed on a heating plate at 90 °C to ensure complete evaporation of the solvents. The ink was sonicated in an ultrasonic bath between the spraying of each layer to maintain the homogeneity of the ink. The platinum loading in the CL was controlled to 0.58 mg Pt $cm^{-2}$ with a PTFE content of 7.8% for cell 1 and 0.50 mg Pt $cm^{-2}$ with a PTFE content of 6.7% for cell 2 and cell 3. Afterward, the GDEs were stamped into square pieces with an area of 2.2 x 2.2 $cm^2$.

Subsequently, three single cells were assembled with the described GDEs as anode and cathode. The active cell area was controlled by a polyether ether ketone (PEEK) subgasket to 4 $cm^2$ between the membrane and each electrode. PTFE gaskets (thickness: 150 μm) were employed as sealing between the electrodes and the stainless-steel endplates with serpentine flow channels.

### 2.2. Electrochemical characterization

The cells were subsequently operated in a test station. Two heating pads on the outer side of each end plate controlled the cell temperature, measured by two thermocouples inserted into the center of each endplate. The accurate gas flow of all utilized gases ($H_2$, $N_2$, $CO_2$, CO) was ensured by mass flow controllers. The gas concentrations are given in vol % at standard conditions. The generated gas mix was preheated by heating coils and channeled through a humidifier before being fed to the anode. No gas flow was applied to the cathode. The anode and the cathode were not pressurized and thus operated under nearly ambient pressure. The pressure at the anode inlet was logged with a pressure gauge to identify potential pressure fluctuations, although none were detected. After heating a cell (schematic representation see Fig. 1) to 160 °C under pure $N_2$ gas flow on the anode, it was conditioned for 48 h with pure $H_2$ at 200 mA $cm^{-2}$ with a humidifier temperature of 30 °C, which corresponds to approximately 0.7% RH at 160 °C. The $H_2$ gas flow was always set to at least 3.75 ml $min^{-1}$ $cm^{-2}$ ($\lambda_{H2} = 2.7$ at 200 mA $cm^{-2}$) for cells 1 and 3 and to 2.50 ml $min^{-1}$ $cm^{-2}$ ($\lambda_{H2} = 1.8$ at 200 mA $cm^{-2}$) for cell 2, except when indicated otherwise. Lower gas flows would create uneven distribution across the membrane electrode assembly, negatively influencing the EIS data quality.

Subsequently, galvanostatic impedance measurements were performed with a Zennium potentiostat (Zahner Elektrik, Germany) at different operating parameters. To monitor high-frequency processes accurately and prevent inductive artifacts, minimizing the formation of magnetic fields around the cabling is essential. By twisting the voltage sensors and the current conductors separately, magnetic fields develop in opposing directions due to opposing current flows. Subsequently, both magnetic fields cancel each other, reducing inductive behavior. Since every additional component in the measurement setup potentially causes inductive artifacts, the potentiostat cables were plugged directly into the endplates. Electrochemical impedance spectra were recorded

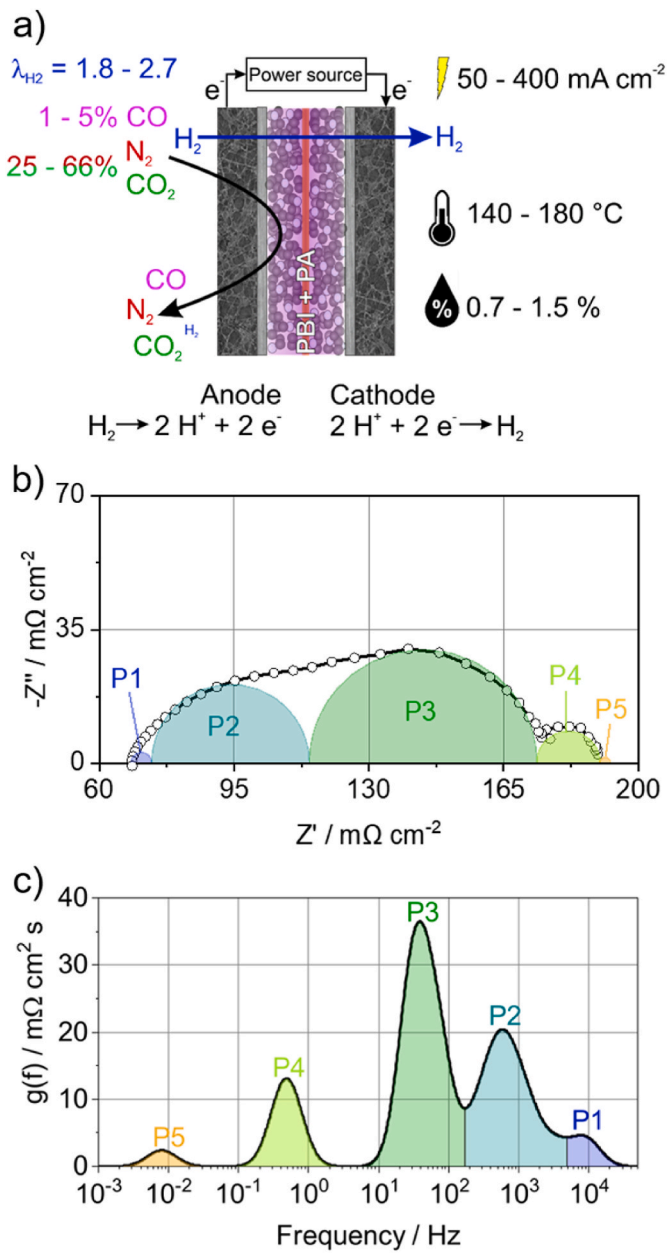


**Fig. 1.** a) Schematic representation of an EHP consisting of a PBI membrane sandwiched between the PA-invaded anode and cathode GDEs based on Pt/C and PTFE. b) Exemplary impedance spectrum with indicated processes extracted from c) the corresponding DRT. The operating parameters of this study are displayed on both sides of the schematic cell.

over the frequency range from 50 mHz to 200 kHz at various current densities, cell temperatures, humidifier temperatures, flow rates, and concentrations of the different gas contaminants. Nearly constant conditions across the cell are assumed due to its low surface area of only 4 cm$^2$. Thus, each process occurs over a narrow frequency range.

Steady-state conditions were assured by waiting until a stable voltage was reached, but always at least 30 min. After changing the gas composition, the waiting period was extended to at least 60 min to saturate the water in the humidifier with the partial pressures of the new gas mix. A stabilization period of 3 days was employed after changing the RH.

The system's stability and data quality was validated with the Kramers-Kronig (KK) transformation performed with the software Lin-KK [18,36]. Selected KK test results at different gas compositions are displayed in the supporting information (Fig. S. 1). Especially at high current densities around 1 Hz the data is noisy. However, no systematic error or drift could be observed, validating the system's stability during EIS measurements. Only clear outliers were deleted (maximum one point per measurement).

12.5 mA cm$^{-2}$ was chosen as amplitude for EIS measurements at 50 mA cm$^{-2}$ DC, while 25.0 mA cm$^{-2}$ was applied in all other measurements. The weighted harmonics autocorrelation algorithm of the Zahner software checked the linearity of the data [37]. The determined significance was above 0.999 for all measurements with pure $H_2$, above 0.991 for the measurements with $H_2$ diluted by $N_2$ or $CO_2$, and above 0.990 for $H_2$ contaminated with CO. These values confirm the linearity of the recorded impedance spectra and suggest good data quality. However, one measurement ($H_2$ + 5% CO/350 mA cm$^{-2}$ at 160 °C performed on cell 1) displayed several data points below a significance of 0.990 at low frequencies, with 0.972 being the lowest.

### 2.3. Distribution of relaxation times

Recorded impedance spectra were transformed into a DRT function with the software Relaxis3 (rhd Instruments, Germany). Only data points between 100 kHz and 50 mHz were utilized for the DRT transformation. Interpreting impedance spectra is often complex due to overlapping effects and nonideal processes. The DRT approach supports the evaluation of EIS by fitting impedance data with an infinite number of RC-elements connected in series with an ohmic resistance [22,38]. However, every measurement exhibited data points that showed inductive behavior in the selected frequency range. An inductor was added to the model to guarantee accurate results at high frequencies. Each peak in the DRT function represents a physicochemical process, and the area under the respective peak represents its resistance.

Calculating the DRT function g(f) is an ill-posed mathematical problem and therefore requires the selection of a regularization parameter λ, which has to be carefully chosen to obtain meaningful results [19,38]. An improperly selected regularization parameter might cause oscillations and false peaks or merge several processes into a single peak. The following section will describe the procedure for selecting the regularization parameter, which can also be applied to other electrochemical systems.

## 3. Results

### 3.1. Selection of the regularization parameter

The number of peaks and their shape in a DRT spectrum depends on selecting the regularization parameter λ [19,20,38]. Fig. 2 presents the DRTs of the same measurement calculated with different regularization parameters. With decreasing regularization parameters, the DRT calculation represents the measured data more accurately, resulting in sharper peaks. However, a very low regularization parameter creates artificial peaks caused by measurement uncertainty. Therefore, a typical strategy is to lower λ until the sum of square residuals (SSR) between the measured EIS and the impedance spectrum reconstructed from the DRT stops decreasing [20].

Only two tilted peaks are visible for $\lambda = 10^{-1}$. Comparing the impedance spectrum reconstructed from DRT with the measured data reveals an inaccurate fit (SSR = 5.3 * $10^{-6}$). The residuals show oscillations, which is typical for not properly fitted data.

At $\lambda = 10^{-3}$, four peaks are visible. The reconstruction accurately overlaps with the measured data in the high and medium frequency range. However, below 1 Hz significant residuals are observed. The residuals are scattered randomly in the positive and negative directions, which suggests that they are caused by noise. Cell voltage fluctuations influence the EIS data mainly in the low-frequency range. As the recording time for each point increases with decreasing frequency, the occurrence of a voltage spike becomes more likely. While reliable DRT

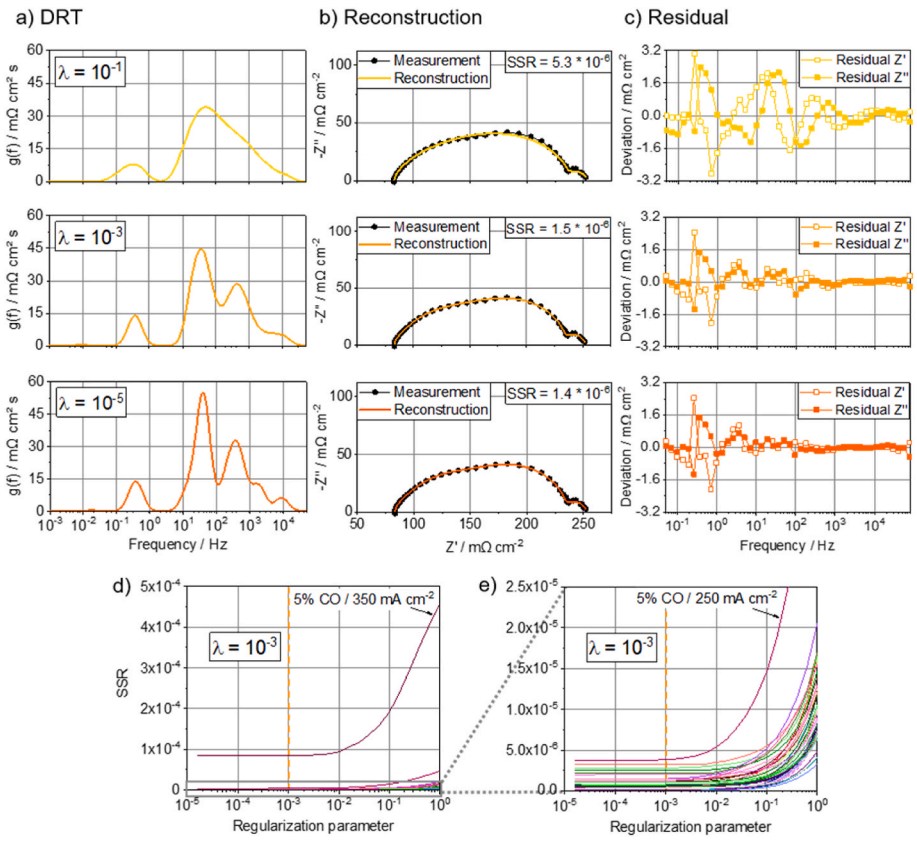


**Fig. 2.** a) DRTs calculated from the same EIS measurement at different regularization parameters, b) corresponding reconstructed impedance spectra compared to the measured data, and c) residuals between the measurement and the reconstruction. d) SSR between the measured EIS data and the impedance spectrum reconstructed from DRT at different regularization parameters for all measurements of cell 1, and e) enlarged section of d). The chosen regularization parameter $\lambda = 10^{-3}$ is indicated.

interpretation is also possible in the low-frequency range, it has to be kept in mind that the resolution is lower than for the high and medium frequencies.

An additional peak appears at 2 kHz when the regularization parameter is further decreased to $\lambda = 10^{-5}$. The nearly unchanged SSR between the measured and the reconstructed EIS data for $\lambda = 10^{-3}$ (SSR $= 1.5 \bullet 10^{-6}$) and $\lambda = 10^{-5}$ (SSR $= 1.4 \bullet 10^{-6}$) and similar residuals suggest that this additional peak is an artifact.

In Fig. 2d and e, the SSR is displayed over the regularization parameter for all measurements performed on cell 1. The SSR decreases with decreasing λ until approximately $\lambda = 10^{-3}$. Slight differences can be observed for different measurements caused by different measurement errors and conditions during each measurement. The SSR of the EIS with 5% CO at 350 mA $cm^{-2}$ is significantly worse than all other measurements since the CO adsorption on the platinum catalyst destabilizes the cell voltage. Voltage fluctuations lead to lower data quality, which makes the DRT analysis of the EIS data challenging. However, the graph still displays the same behavior at different regularization parameters as the other measurements. Further decrease of λ below $10^{-3}$ does not produce a better fit but creates artifacts. Therefore, $\lambda = 10^{-3}$ was chosen as the regularization parameter.

### 3.2. Influence of gas contaminants

Polarization curves, impedance spectra, and the corresponding DRTs of cells 1 and 2 with different anode gas compositions at 160 °C cell temperature and 30 °C humidifier temperature are displayed in Fig. 3. With pure $H_2$, the open circuit voltage (OCV) is 0 mV due to the identical gas composition on the anode and the cathode. $H_2$ dilution with $N_2$, $CO_2$, or CO increases the OCV due to the different anode gas composition, as described by the Nernst equation. $N_2$ and $CO_2$ show a similar influence on the OCV, as shown in Table 1. In the investigated concentration range, the OCV increases nearly linearly with increasing contaminant concentration. Since the partial pressure of the reactants mainly determines the OCV, CO has little influence on the OCV due to the significantly lower concentrations. The cathode gas mix can be assumed to be identical for all anode contaminants since high-temperature $H_2$ pumping produced $H_2$ with a purity >99.4% on the cathode for gas feeds, similar to those applied in this study [11,12,14]. The OCV was nearly identical at the respective gas composition for all tested cells.

With pure $H_2$ gas feed, the voltage increases linearly over the evaluated current density range. Both $N_2$ and $CO_2$ slightly change the slope of the PC, indicating increasing resistances at higher currents. While the low CO concentrations barely influence the OCV (1 mV at 1% CO), they produce a steeper slope. CO adsorption on the platinum catalyst decreases the electrochemically active surface area (ECSA), significantly increasing the EHP's power consumption [11–15].

Impedance spectra recorded at 150 mA $cm^{-2}$ for cell 1 and 200 mA $cm^{-2}$ for cell 2 (Fig. 3c and d) allow the separation of the underlying processes. The low-frequency resistance ($R_{LF}$) in the EIS also represents the total cell resistance ($R_{tot}$) and corresponds to the slope of the PC. The high-frequency resistance ($R_{HF}$), which represents the electronic resistance in the GDEs and the ion conduction resistance of the membrane, is not displayed in the DRT. Typically, the ionic conductivity is significantly smaller than the electronic conductivity. Therefore, the high-frequency intersection of the impedance data with the x-axis can be assumed to represent the membrane resistance ($R_M$). No contaminant influenced the membrane resistance in this study, although a membrane resistance increase under CO contamination was previously demonstrated for a high-temperature PEM FC with a PBI membrane [39].

Five peaks are detected in the corresponding DRTs. The frequency ranges of P1 (~10 kHz), P2 (~1 kHz), and P3 (~70 Hz) are overlapping, which makes their separation difficult. While these three peaks are visible in all measurements for cell 2, P2 and P3 overlap for cell 1. P1 is not influenced by any of the contaminants in both cells. In high-temperature and low-temperature PEM FCs, the proton conductivity in

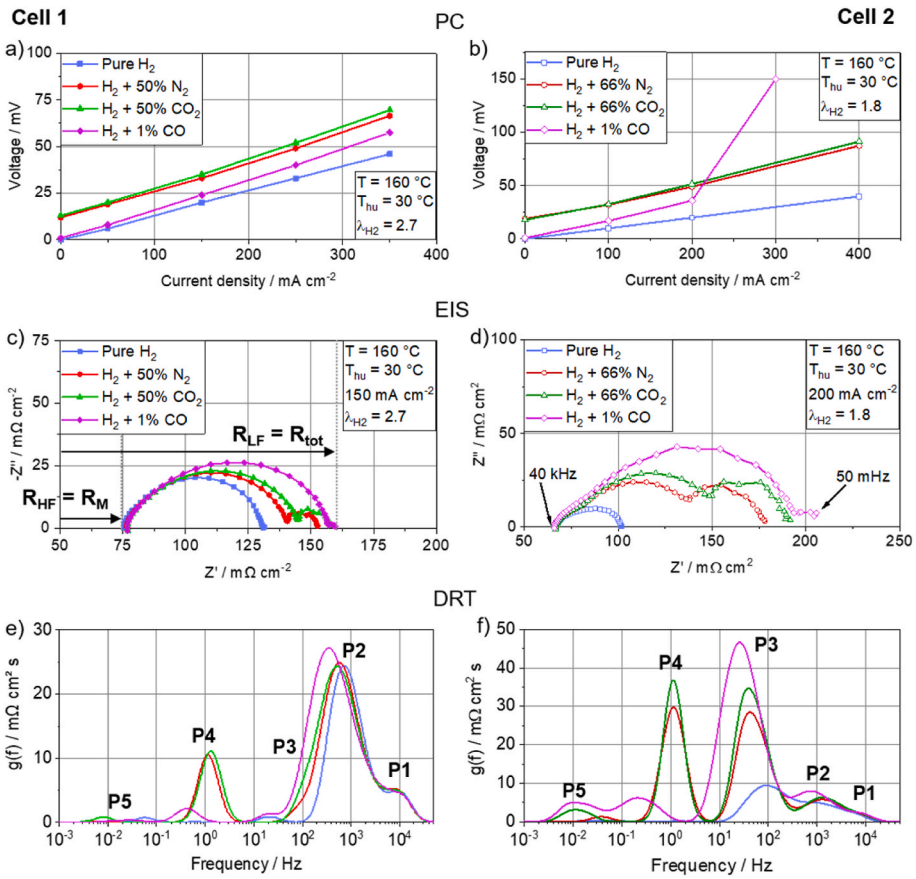


**Fig. 3.** Polarization curves at different anode gas compositions, 160 °C cell temperature, 30 °C humidifier temperature, and a) $\lambda_{H2} = 2.7$ (cell 1) or b) $\lambda_{H2} = 1.8$ (cell 2), EIS recorded at c) 150 mA $cm^{-2}$ (cell 1) and d) 200 mA $cm^{-2}$ (cell 2), and e) and f) the corresponding DRTs.

**Table 1**
Cell OCV at different contaminant concentrations.

| Contaminant | Concentration / % | OCV / mV |
|---|---|---|
| $N_2$ | 33 | 7 |
| | 50 | 12 |
| | 66 | 19 |
| $CO_2$ | 33 | 8 |
| | 50 | 13 |
| | 66 | 18 |
| CO | 1 | 1 |
| | 5 | 2 |

the GDEs can be observed at high frequencies [20,21]. Furthermore, the chosen contaminants should not affect the electrode's proton conductivity, which suggests that P1 represents the proton transfer in the GDEs. Additionally, a decrease of P1 at increasing temperature and humidification will later be discussed in Figs. 6 and 7. Since increasing temperature and water content improve the proton conductivity of PA, this observation further strengthens the peak assignment of P1 to the proton conduction in the electrode.

P2 increases slightly in cell 2 with all contaminants compared to pure $H_2$. Integrating the area under P2 for cell 2 gives 10.0 mΩ $cm^2$ for pure $H_2$, 11.0 mΩ $cm^2$ for 66% $N_2$, 12.7 mΩ $cm^2$ for 66% $CO_2$ and 17.4 mΩ $cm^2$ for 1% CO contamination. However, selecting the integration boundaries is difficult due to the overlapping of P2 with P1 and P3, which makes precise resistance determination difficult. Since the cathode conditions are unchanged, P2 is attributed to the hydrogen evolution reaction (HER) on the cathode side. Diffusion of the contaminants through the membrane to the cathode might increase the HER resistance slightly. The different P2 shape is caused by a change in P3, which increases and shifts to lower frequencies for all contaminants (90 Hz for pure $H_2$, 40 Hz for 66% $N_2$ and $CO_2$, 25 Hz for 1% CO in cell 2). Only the anode is poisoned, which suggests that the growing P3 can be attributed to the anode, most likely to the hydrogen oxidation reaction (HOR). Primarily CO contamination inhibits the HOR due to the CO adsorption on platinum, significantly lowering the ECSA. $CO_2$ influences the HOR more than $N_2$ at identical concentrations. Higher $CO_2$ solubility in water compared to $N_2$ could displace dissolved $H_2$ in the electrolyte [40]. Lower $H_2$ concentration at the triple-phase boundaries hamper the HOR, as described in the Butler-Volmer equation [41]. When a high-temperature PEM FC is fed with humidified $H_2$ and CO, the CO is partially converted to $CO_2$ in a water-gas-shift reaction on the platinum catalyst [42].

$$CO + H_2O \rightleftharpoons CO_2 + H_2 \quad (1)$$

The operating conditions in the EHP favor the formation of CO, since the RH is low while the partial pressures of $CO_2$ and $H_2$ are high. Furthermore, cyclic voltammetry revealed adsorbed CO on the Pt catalyst of a Nafion-based EHP fed with $H_2$ and $CO_2$ [43]. The chemical reduction of $CO_2$ to CO in the EHP was identified as the underlying mechanism for CO formation. Therefore, small amounts of formed CO might also increase the cell resistance with $CO_2$ gas feed in the investigated high-temperature EHP. Thus, $CO_2$ lowers HOR activity more than $N_2$ at identical concentrations. Further data supporting these peak assignments will be presented in the following sections.

In cell 1, P2 and P3 are not separable for pure $H_2$, but a shoulder appears at the lower frequency edge (~100 Hz) for all contaminants, which represents the increasing P3 that was observed separately for cell 2. Slightly higher platinum loading in cell 1 (0.58 mg Pt $cm^{-2}$) seems to

improve the HOR significantly compared to cell 2 (0.50 mg Pt $cm^{-2}$) since P3 is significantly smaller and consequently merges with P2 in the DRT of cell 1. Especially under CO contamination, cell 2 performs worse, showing a substantial increase of P3 compared to cell 1. High catalyst loading is, therefore, especially beneficial for good HOR kinetics at challenging gas contaminants like CO.

P4 appears at approximately 1 Hz with $N_2$ and $CO_2$ contamination and can be ascribed to the mass transport (MT) resistance. For pure $H_2$ and with 1% CO, a small peak at 20 Hz can be observed in cell 1, which might be related to $H_2$ diffusion. Due to the fast diffusion of $H_2$, the MT resistance is small and appears at a high frequency. The impact of $N_2$ and $CO_2$ on P4 is stronger than the effect of CO. Higher concentrations of $N_2$ and $CO_2$ (50% for cell 1 and 66% for cell 2) compared to CO (1%) increase the hydrogen diffusion pathway in the gas phase, which causes a MT resistance increase. Catalytic sites blocked by CO also present a diffusion resistance for $H_2$ since the pathway to the remaining active sites increases. The frequency of approximately 1 Hz for P4 is nearly identical to the MT process in a typical high-temperature PEM FC, which further supports the assignment of P4 to the MT [21]. P4 appears at slightly lower frequencies with CO compared to $N_2$ and $CO_2$. Different diffusion phenomena dominate depending on the contaminant, resulting in a frequency shift. For $N_2$ and $CO_2$ the gas phase diffusion in the porous CL could be the dominating factor, while with CO, the diffusion of dissolved $H_2$ through the PA electrolyte to the significantly fewer active catalyst sites might be more relevant. This issue could explain why with 1% CO in cell 1, two diffusion peaks can be observed at 20 Hz and 400 mHz, respectively. The diffusion in the gas phase (20 Hz) is nearly identical to pure $H_2$ due to the small contaminant concentration. The subsequent diffusion step in the liquid PA to the catalytic sites is strongly inhibited and poses the main barrier for the MT.

Since inhibition of the gas diffusion also influences the following reaction, the increase of the HOR resistance (P3) with $N_2$ and $CO_2$ contamination could be linked to the hampered MT [44]. Identical trends for P4 were observed for both cells since the platinum loading typically only has a minor influence on the MT resistance [45]. P5 will be discussed in the following section.

$N_2$ and $CO_2$ are similarly influencing the performance. Therefore, in this study, we present only the impedance spectra and the corresponding DRTs from the $CO_2$ measurements. The $N_2$ data consistently shows slightly lower resistances at identical operating parameters, which could be attributed to smaller P3 and P4 in the DRT.

### 3.3. Influence of current density

Fig. 4 presents EIS measurements at different current densities and the corresponding DRTs for different gas compositions. No influence of the current density on the membrane resistance and the proton conductivity in the electrodes (P1) was observed.

No significant total resistance change is observed in the impedance spectrum for pure $H_2$, which agrees with the linear PC in Fig. 3. However, the increasing current seems to reduce the resistance slightly, which can be attributed to decreased overlapping P2 and P3. Increased

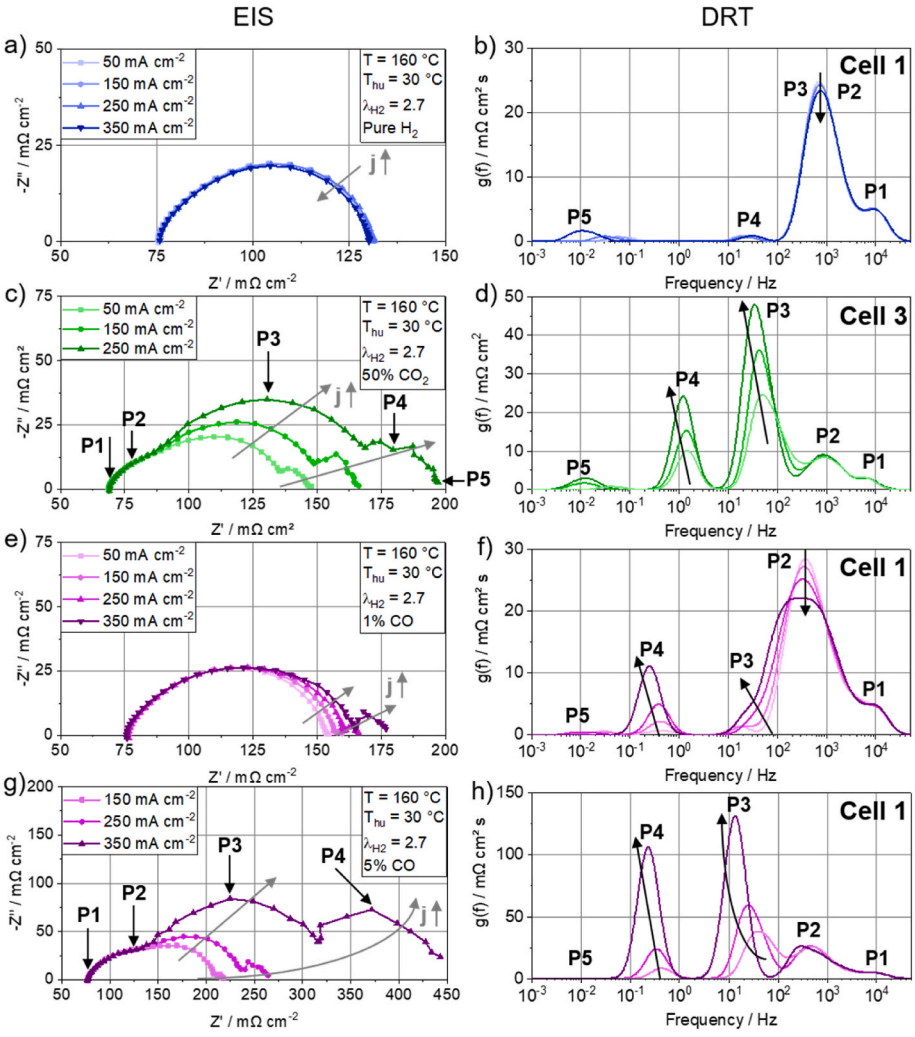


**Fig. 4.** Current density variation: a) impedance spectra and b) corresponding DRTs of cell 1 with pure $H_2$, c) impedance spectra and d) corresponding DRTs of cell 3 with $H_2$ + 50% $CO_2$, e) impedance spectra and f) corresponding DRTs of cell 1 with $H_2$ + 1% CO, and g) impedance spectra and h) corresponding DRTs of cell 1 with $H_2$ + 5% CO (160 °C cell temperature, 30 °C humidifier temperature, $\lambda_{H2}$ = 2.7). The characteristic frequency of each process determined from the DRT peaks is marked in the impedance spectra for the measurements at 50% $CO_2$ at 250 mA $cm^{-2}$ (c) and 5% CO at 350 mA $cm^{-2}$ (g).

reaction rate at higher currents might slightly elevate the cell temperature, improving the reaction kinetics. Furthermore, phosphate anion migration into the anode is enhanced at increasing current density [46,47]. This effect decreases the ohmic resistance in the anode GDE while increasing the ohmic resistance in the cathode of an $H_2$ pump [48]. Increased PA content in the anode could improve the HOR kinetics, which explains the slightly decreasing impedance at a higher current. Furthermore, charge transfer resistances usually depend on the potential. The higher overpotential at increasing current density might facilitate the occurring reactions.

P3 separates from P2 by shifting to lower frequencies at increasing current density for 50% $CO_2$, 1% CO and 5% CO contamination. The current density does not influence P2 with 50% $CO_2$ in cell 3. Furthermore, data from cell 2 presented in the supporting information (Fig. S. 2) also indicates no change of P2 under 1% CO at varying current density. With 5% CO in cell 1 the shape of P2 is impacted by the frequency change of P3, and the integrated area under P2 is slightly increasing (54.8 mΩ $cm^2$ at 150 mA $cm^{-2}$, 61.2 mΩ $cm^2$ at 350 mA $cm^{-2}$). In contrast, P2 decreases with increasing current density under 1% CO for cell 1 (Fig. 4f). This apparent trend is caused by an increase and a shift of P3 to lower frequencies, as observed in the other measurements, and the increase of P3 overcompensates the apparent P2 decrease. The combined integrated area below P2 and P3 increases from 73.1 mΩ $cm^2$ at 50 mA $cm^{-2}$ to 83.8 mΩ $cm^2$ at 350 mA $cm^{-2}$ at 1% CO. Individual steps influence other parts as all processes are coupled in electrochemical systems. Inhibition of the anode reaction by 5% CO also impacts the HER on the cathode, although significantly smaller. This issue causes a slight increase of P2 at 5% CO, but not at lower contaminant concentration. Fig. 3f already showed CO contamination increasing P2 in cell 2 as well. Thus, only at a high contaminant concentration P2 shows a dependency on the current. Likewise, CO poisoning of the anode of a high-temperature PEM FC also provoked a resistance increase of the oxygen reduction reaction on the cathode [21].

5% CO contamination results in the separation of P2 from P3 due to the limited HOR activity, which shifts P3 to a lower frequency. Consequently, both peaks appear individually in the corresponding DRT. P3 can also be observed separately at 50% $CO_2$ contamination in cell 3. P3 substantially increases at higher current density in both cases, for CO and $CO_2$ in the anode gas feed, due to the hampered HOR.

The current density does not influence the MT peak P4 at 20 Hz for pure $H_2$. Without contamination, $H_2$ diffusion is fast enough only to pose a minor, current-independent resistance in the EHP. Contrarily, the corresponding low-frequency EIS semicircle enlarges at higher current densities for all measurements with contaminants in the gas feed. An increased reaction rate at a higher current requires higher reactant diffusion to the catalytically active centers, which increases the MT resistance. The corresponding DRT peak P4 increases and shifts to slightly lower frequencies. Similarly, increased diffusion resistance at higher currents was also observed for oxygen gas transport in PEM FCs [20,21].

P5 appears at very low frequencies between 10 mHz and 100 mHz, at the lower end of the measured frequency range (>50 mHz). While it might be an artifact caused by lower data quality at low frequencies due to voltage fluctuations, an increase of P5 with increasing current density was detected in several measurement series under different gas compositions (Fig. 4a–d, Fig. S. 2). P5 might represent PA ion movement from the cathode to the anode. A part of the current in high-temperature PEM FCs is balanced by PA ions migrating from the cathode to the anode since most PA molecules are mobile in the cell. It was shown that this effect increases at higher current densities [47]. Similar frequencies were previously observed for ion movement in vanadium redox flow battery electrolytes [31]. Since P5 only poses a minor contribution to the total resistance, its reliable measurement is insignificant and will not be discussed in the following.

### 3.4. Influence of contaminant concentration and stoichiometry

Fig. 5 presents impedance spectra and the corresponding DRTs of cell 1 at different $CO_2$ and CO concentrations at 160 °C cell temperature, 30 °C humidifier temperature and 150 mA $cm^{-2}$ for $CO_2$, and 250 mA $cm^{-2}$ for CO. The $CO_2$ concentration affects the HOR and the MT resistance. Since the adsorption of gases in liquids is driven by partial pressures, these results support the previous assumption that $CO_2$ dissolution in PA inhibits the HOR. Increasing CO concentration hampers the HOR activity (P3) and the diffusion (P4) even more so. CO coverage of the platinum catalyst increases with increasing CO partial pressures [49]. A lower ECSA inhibits the HOR and increases the diffusion pathway of $H_2$ since fewer sites are available. The combined charge transfer resistance of HOR and HER (P2 and P3) increases linearly over the examined gas concentration ranges for both gases. CO causes a significantly higher resistance increase with 19.1 mΩ $cm^2$ per % of CO compared to only 0.1 mΩ $cm^2$ per % of $CO_2$. A linear increase can also be observed for the MT resistance (P4) for $CO_2$ contamination with 0.2 mΩ $cm^2$ per % $CO_2$. Therefore, approximately two-thirds of the total resistance increase with $CO_2$ is caused by diffusion limitations. At 0% $CO_2$, which means pure $H_2$, an MT resistance of 2.5 mΩ $cm^2$ is obtained by extrapolating the performed linear fit. Pure $H_2$ measurements showed an MT resistance of 1.1 mΩ $cm^2$, which is close to the value obtained by the extrapolation of the linear fit for varying $CO_2$ concentrations. The excellent agreement of both values suggests an almost linear MT increase with increasing $CO_2$ partial pressure over the entire concentration range. With CO in the anode gas feed, the MT resistance increased exponentially. While the charge transfer resistance was dominant in the investigated parameters, the MT resistance could become the main contributor if gas with high CO content, such as syngas, is fed to the EHP.

Furthermore, a minor increase in P2 is observed with CO and $CO_2$ in the gas feed. As discussed previously, the coupling of all processes affects the HER on the cathode as well if the anode is poisoned.

Increased stoichiometry does not influence the impedance spectrum for operation with pure $H_2$. The DRTs are identical at different $H_2$ gas flows (EIS and DRT presented in the supporting information: Fig. S. 3). This supports the previous assumption that $H_2$ transport poses no limitation under these conditions. With 50% $CO_2$, a decrease in the total resistance is observed at increasing gas flow, which can be solely attributed to a decrease in P4. Therefore, higher gas stoichiometry can potentially lower cell power consumption. However, this would lead to a lower $H_2$ recovery rate. Both factors need to be taken into account when choosing suitable flow rates. These results support the assignment of P4 to the mass transport, which decreases at higher stoichiometry due to the increased amount of reactants.

When operating the EHP with CO, no difference in the total resistance was measured at different $H_2$ stoichiometries. The EIS and DRT data reveal that the MT resistance P4 decreases at higher gas flows analog to the $CO_2$ data. However, this resistance decrease is compensated by an increase of P3. An increased gas flow transports more CO into the cell. Subsequently, more ECSA is blocked by CO, which decreases the HOR activity. Thus, increasing gas flow does not improve cell performance under 1% CO contamination. Concentrations above 1% CO might even reduce cell performance when the stoichiometry increases.

### 3.5. Influence of temperature and humidification

Increasing temperature decreases CO adsorption on platinum, which is an efficient way to improve the performance significantly, as shown in the following section. However, it has to be considered that the long-term stability of PA-doped PBI severely degrades at 180 °C [50,51]. Fig. 6 depicts EIS and DRT spectra of cell 1 at cell temperatures from 140 °C to 180 °C at 30 °C humidifier temperature and $\lambda_{H2} = 2.7$ with different anode gas compositions. The corresponding resistances extracted by integrating the DRT peak areas are presented in Fig. 8b, c, and e. The proton conduction in the electrodes (P1) improves by raising

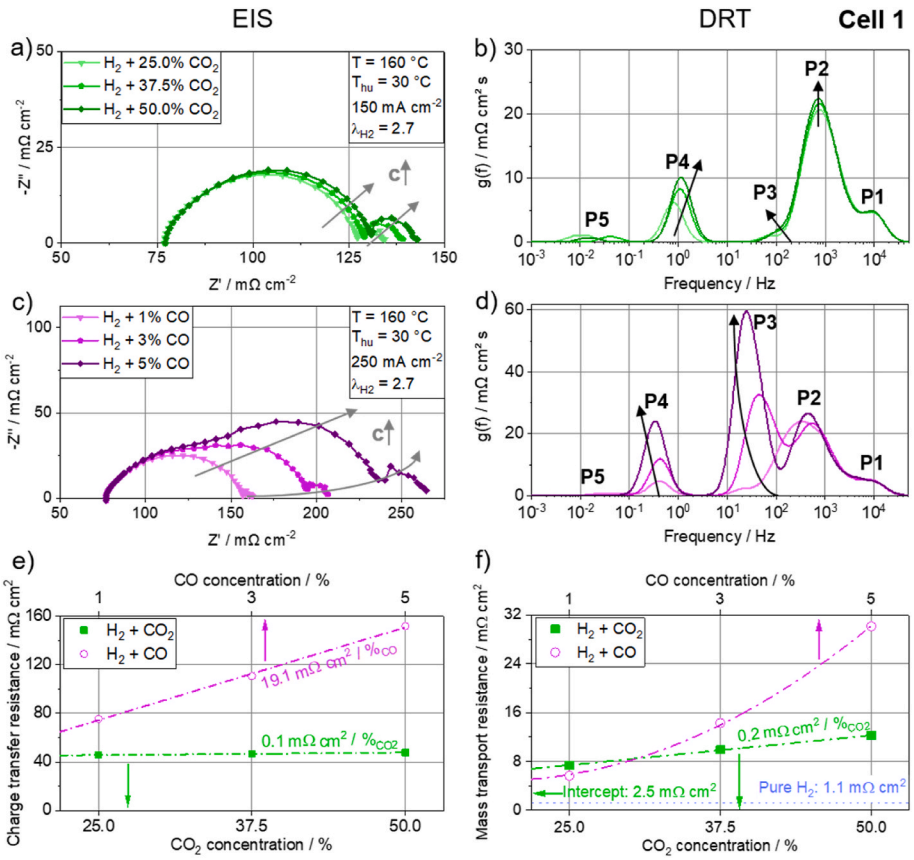


**Fig. 5.** Contaminant concentration variation performed on cell 1: a) impedance spectra and b) corresponding DRTs at 150 mA $cm^{-2}$ with $H_2 + CO_2$, and c) impedance spectra and d) corresponding DRTs at 250 mA $cm^{-2}$ with $H_2 + CO$ (160 °C cell temperature, 30 °C humidifier temperature, $\lambda_{H2} = 2.7$). e) Charge transfer resistance (P2 + P3) and f) mass transport resistance (P4) dependency on the contaminant concentration. The resistances were extracted by integration of the area under the respective peaks.

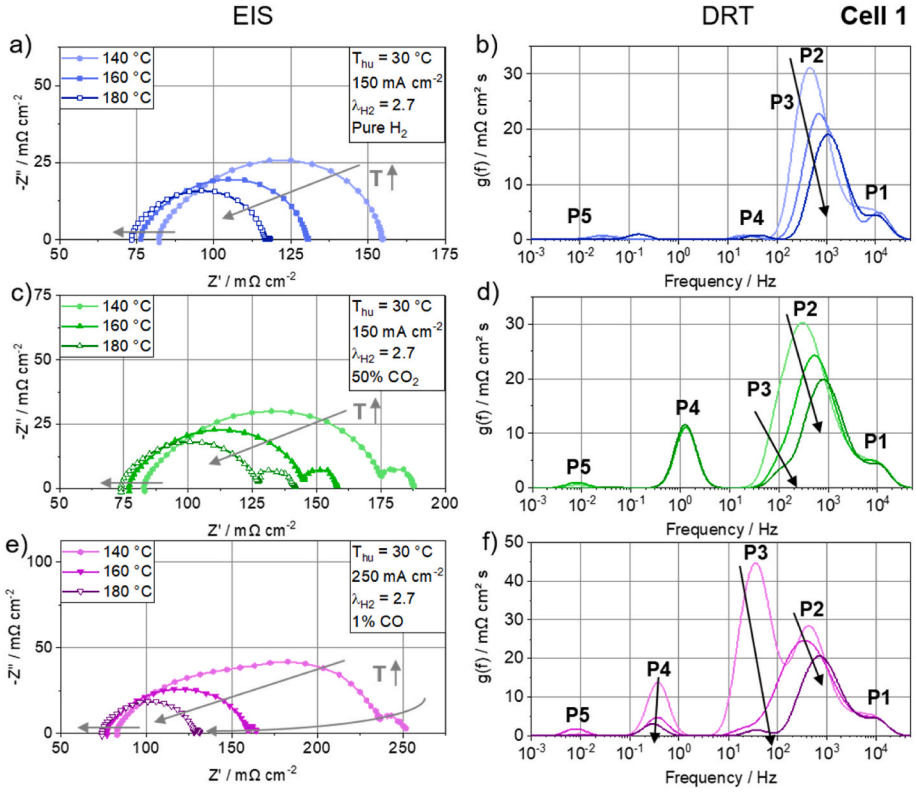


**Fig. 6.** Temperature variation performed on cell 1: a) impedance spectra and b) corresponding DRTs at 150 mA $cm^{-2}$ with pure $H_2$, c) impedance spectra and d) corresponding DRTs at 150 mA $cm^{-2}$ with $H_2$ + 50% $CO_2$, and e) impedance spectra and f) corresponding DRTs at 250 mA $cm^{-2}$ with $H_2$ + 1% CO (30 °C humidifier temperature, $\lambda_{H2} = 2.7$).

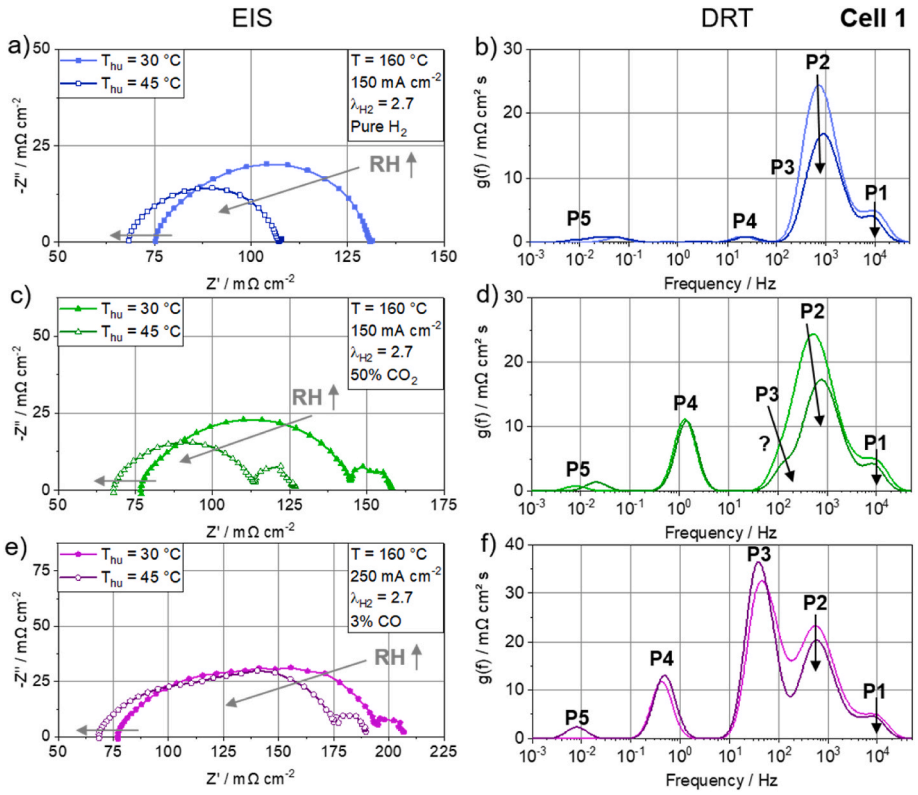


**Fig. 7.** RH variation performed on cell 1: a) impedance spectra and b) corresponding DRTs at 150 mA $cm^{-2}$ with pure $H_2$, c) impedance spectra and d) corresponding DRTs at 150 mA $cm^{-2}$ with $H_2$ + 50% $CO_2$, and e) impedance spectra and f) corresponding DRTs at 250 mA $cm^{-2}$ with $H_2$ + 3% CO (160 °C cell temperature, 30 °C humidifier temperature, $\lambda_{H2} = 2.7$).

the temperature from 140 °C to 180 °C (see Fig. 8b) since PA exhibits better proton conductivity at a higher temperature [52].

The better performance is linked to smaller P2 and P3 peaks since higher temperatures improve the HOR (P3) and the HER (P2) reaction kinetics. In the supporting information, EIS and DRT data of cell 3 (Fig. S. 4) show a decrease of the separated P2 and P3 with increasing temperature for pure $H_2$ and $H_2$ + $CO_2$. The diffusion (P4) remains unchanged using pure $H_2$ and $H_2$ + $CO_2$ since the gas phase diffusion is typically only slightly influenced by the temperature [53]. While the diffusion rate increases at a higher temperature, the gas solubility in the liquid electrolyte decreases. Both effects impact the diffusion resistance and depend on the cell temperature and the RH [50]. Both effects compensate each other in the investigated parameter range.

With CO in the gas feed, increasing operating temperature significantly decreases the resistance for P2, P3, and P4. At elevated temperatures, CO desorption from the platinum surface is favored, thereby increasing the ECSA and reducing the $H_2$ diffusion pathway. Compared to pure $H_2$, 1% CO in the gas feed increases the cell power consumption by 26% at 160 °C and only by 11% at 180 °C. Since the temperature does not impact the diffusion resistance (P4) for $CO_2$, the performance boost at 180 °C is significantly smaller than with CO contamination. At 180 °C, the charge transfer resistance for 1% CO, 50% $CO_2$, and 50% $N_2$ contamination is similar (see Fig. 8c).

Therefore, a high operating temperature is especially beneficial for operations with high CO concentrations in the gas feed. Membranes and ion-conducting binders, which tolerate operation up to 220 °C are currently under investigation, potentially enabling hydrogen separation from syngas with up to 40% CO [14,35].

PBI-based EHPs are typically operated with humidified gas feed to boost performance [11–13]. In Fig. 7, the influence of different RHs is investigated for pure $H_2$, and $H_2$ contaminated with $CO_2$ or CO in cell 1 at 160 °C and $\lambda_{H2} = 2.7$. 30 °C and 45 °C humidifier temperature correlate to approximately 0.7% and 1.5% RH at 160 °C, respectively. The corresponding resistances extracted by integrating the DRT peak areas are summarized in Fig. 8b, d, and f.

This RH increase shows a substantial reduction of the membrane resistance at 9% compared to the previously presented reduction of only 4% observed when increasing the cell temperature from 160 °C to 180 °C (see Fig. 8a). The average membrane resistance and the corresponding standard deviation were calculated for all impedance spectra presented in Figs. 6 and 7, as well as for the EIS data recorded with $H_2$ + 50% $N_2$. Furthermore, an increased RH also improves the proton conductivity in the GDEs represented by P1 (see Fig. 8b). PA shows optimum proton conductivity in concentrated (85%) PA at 160 °C [52,54]. Low humidification and high temperature cause the dehydration to isolate phosphorous pentoxide, while high RH dilutes the electrolyte, slowly approaching the lower proton conductivity of water. Thus, humidification is essential to maintain an optimal PA state and high proton conductivity.

Elevated RH also reduces the HER (P2) resistance significantly. Humidified PA releases more protons, which shifts the HER reaction equilibrium to the product side:

$$2\,H^+ \rightleftharpoons H_2 \tag{2}$$

Higher proton concentration favors the evolution of $H_2$, which decreases the HER resistance. Furthermore, improved electrolyte distribution due to the lower viscosity of PA at higher RH might enhance the triple phase boundary, improving the reaction kinetics. While the shape of P3 changes for different RHs, the integrated area below the DRT peak stays constant for CO (see Fig. 8d). Since P3 is not separable from P2 for pure $H_2$ and $H_2$ + $CO_2$, no clear conclusion can be drawn on the HOR behavior at varying RH under these conditions. However, the CO results suggest humidification does not substantially influence the HOR.

P4 is unaffected by the RH for pure $H_2$ and $H_2$ + $CO_2$, which suggests the RH increase does not cause GDE flooding. Flooded pores would

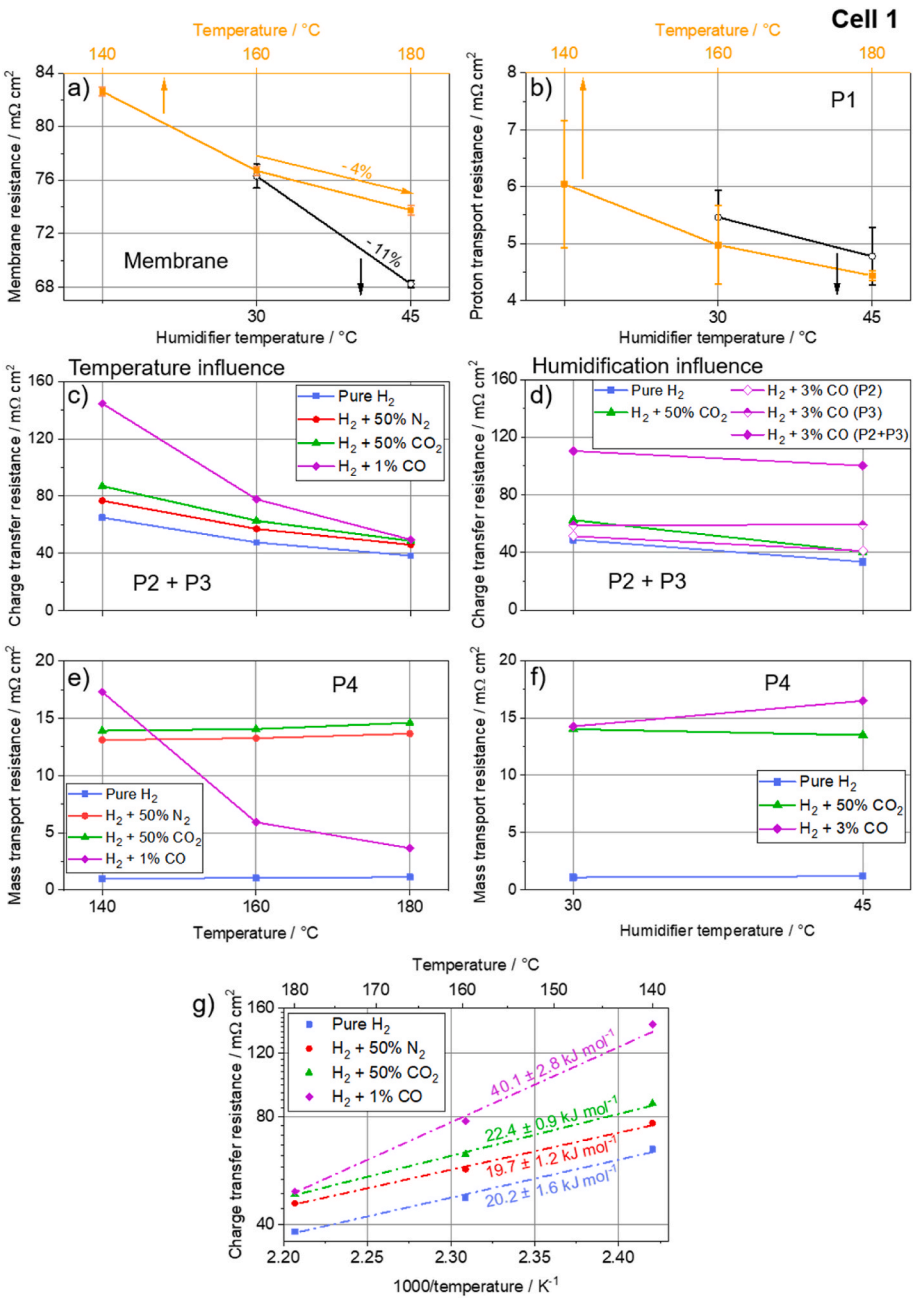


**Fig. 8.** a) Membrane resistance and b) proton transport resistance dependency on the temperature and the RH. Charge transfer resistance dependency on c) the temperature and d) the RH, and the MT resistance dependency on e) the temperature and f) the RH. The resistances were extracted from EIS and DRT data presented in Figs. 6 and 7. For a) and b), average values with standard deviation were calculated. g) Temperature influence on the combined HOR and HER charge transfer resistance with linear Arrhenius fit.

increase the MT resistance since the reactant diffusion in PA is significantly slower than in the gas phase [55–57]. However, a slight MT resistance increase was detected with 1% CO. Higher RH increases the liquid electrolyte content in the GDEs, since the hygroscopic PA partially absorbs the additional humidity. This effect increases the thickness of the PA layer covering the porous electrode structure. A longer diffusion pathway through the electrolyte increases the MT resistance. This effect might not appear for $CO_2$ contamination since the primary diffusion occurs in the gas phase. Since most of the ECSA is still available, the diffusion in liquid PA has only a minor contribution compared to CO contamination. Therefore, the RH has no significant effect on the diffusion with $CO_2$.

For $CO_2$ in the gas feed, the RH increase boosts the performance more substantially than the previously presented temperature increase, while the opposite behavior is observed for CO. The more pronounced decrease of the proton conductivity in the membrane and the GDEs at high RH is outweighed by the HOR and MT improvements due to the reduced CO adsorption at 180 °C. Therefore, optimized humidification is essential when the EHP is operated under pure $H_2$ (as a compressor) or with $CO_2$ and $N_2$ in the gas feed.

PA is highly hygroscopic, which causes flooding of the GDEs at high gas flow and elevated RH [58]. An extreme MT resistance increase was measured by EIS at high RH, especially with a high membrane doping level (see supporting information: Fig. S. 5). Therefore, optimal acid management is essential for stable and efficient cell operation. Since many parameters influence the PA distribution (membrane material, PA doping level, hydrophobicity of binder material, binder content in the GDEs, GDE pore structure, cell temperature, gas flow), no universal RH can be assessed as appropriate for every type of cell. High water production in high-temperature PEM FCs accelerates degradation due to the lower electrolyte viscosity, which causes PA leaching from the cell [59]. The RH of the gas feed has a similar effect. Therefore, cell degradation also has to be considered when selecting the RH.

Fig. 8g presents the Arrhenius diagram of the combined charge

transfer resistances of the HOR and the HER (P2 + P3) with different gas compositions, which were extracted from the EIS and DRT data of Fig. 6. It was impossible to study both reactions individually since the processes could not be separated in the DRTs spectra due to their similar frequencies. The total kinetic resistance is well approximated by a linear fit performed in Relaxis3, demonstrating Arrhenius's behavior and further supporting the assignment of P2 and P3 to the charge transfer reactions. The slope indicates an activation energy of $20.2 \pm 1.6$ kJ mol$^{-1}$ for pure $H_2$. This value agrees with literature results for the HOR activation energy in an acidic environment [60], although no results describe the HOR in pure PA as for the EHP in this study. $CO_2$ and $N_2$ contamination do not influence the activation energy significantly, and the determined fit errors overlap with the value determined for pure $H_2$. Despite similar activation energy, the charge transfer resistance increases with $N_2$ and $CO_2$ contamination due to different partial pressures at the catalyst, as described in the Butler-Volmer equation [41]. However, CO contamination doubles the activation energy, indicating hindering of the charge transfer reactions or occurring side reactions.

## 4. Conclusion

The influence of different anode gas compositions on the EHP was investigated by DRT analysis. A variation of the operating conditions (current density, temperature, humidification, contaminant concentration, $H_2$ stoichiometry) resulted in changes in the impedance, which were utilized to assign the DRT peaks to physicochemical processes. Four processes were identified in the DRT spectra, which were assigned to the proton transport in the electrode (~10 kHz), the HER (~1 kHz), the HOR (~70 Hz), and the mass transport (~1 Hz). A fifth peak at a low frequency (<100 mHz) was detected unreliably but might correspond to the phosphate anion movement from the cathode to the anode. To our knowledge, this study represents the first DRT analysis of an EHP. Furthermore, the paper presented a method to select an appropriate DRT regularization parameter.

Operation with pure $H_2$ on the anode resulted in a nearly linear PC. Contamination of the gas feed with $N_2$, $CO_2$ or CO increased the power consumption of the EHP and caused a nonlinear PC with a steeper slope at increasing current density. Increasing total cell resistance in the corresponding EIS and DRT data confirms the PC results. While almost no change in the EIS was detected at different currents for pure $H_2$, the HOR and the MT resistances increased under the influence of all contaminants. A slight increase in the platinum loading from 0.50 mg Pt cm$^{-2}$ to 0.58 mg Pt cm$^{-2}$ on the anode and the cathode improved the performance for all gas contaminants, especially with CO.

Increased gas stoichiometry had no performance influence for pure $H_2$, but decreased the mass transport resistance for contamination with $N_2$ and $CO_2$. The other resistances were not affected. With 1% CO, a gas flow change did not influence the total resistance, although an increase in the HOR and a decrease in MT resistance were recorded. However, both effects compensated each other. Thus increasing stoichiometry did not influence the performance in case 1% CO was present in the gas feed. With $CO_2$ an increase in the contaminant concentration in the gas feed leads to a linear resistance increase, mainly linked to HOR and MT. Contrary, an increase in the CO concentration caused an exponential cell resistance increase at 160 °C.

Increased operating temperature improved all physicochemical processes, except for the mass transport, which only improved with CO contamination. Enhanced reaction kinetics, higher proton conductivity, and accelerated CO desorption decreased the EHP's power consumption. Especially for CO, the temperature significantly influenced the cell performance. Increased RH in the gas feed decreased the membrane, proton transfer, and HER resistances. Higher RH increases the proton concentration in the electrolyte, improving the conductivity and the HER. Furthermore, a lower electrolyte viscosity improves the PA distribution in the GDEs, further improving the proton conductivity.

This work demonstrates that DRT is a valuable tool for investigating EHP impedances. It helps identify and quantify cell polarization losses according to their respective time constants-a key finding to derive meaningful equivalent circuits and physical models. Those will generate essential parameters for a successful EHP development.

## CRediT authorship contribution statement

**Michael Braig:** Visualization, Formal analysis, Data curation, Investigation, Methodology, Writing – original draft. **Roswitha Zeis:** Conceptualization, Funding acquisition, Supervision, Writing – review & editing.

## Declaration of competing interest

The authors declare that they have no known competing financial interests or personal relationships that could have appeared to influence the work reported in this paper.

## Data availability

Data will be made available on request.

## Acknowledgment

The authors thank the ZSW (Zentrum für Sonnenenergie und Wasserstoff-Forschung) Ulm for providing the hydrogen test stations infrastructure. This work contributes to the research performed at CELEST (Center for Electrochemical Energy Storage Ulm-Karlsruhe).

## Appendix A. Supplementary data

Supplementary data to this article can be found online at https://doi.org/10.1016/j.jpowsour.2023.233203.

## Glossary

| | |
|---|---|
| $CH_4$ | Methane |
| CL | Catalyst layer |
| CO | Carbon monoxide |
| $CO_2$ | Carbon dioxide |
| ECSA | Electrochemical surface area |
| EIS | Electrochemical impedance spectroscopy |
| FC | Fuel cell |
| DRT | Distribution of relaxation times |
| GDE | Gas diffusion electrode |
| GDL | Gas diffusion layer |
| EHP | Electrochemical hydrogen pump |
| HER | Hydrogen evolution reaction |
| HOR | Hydrogen oxidation reaction |
| $H_2$ | Hydrogen |
| $H_2S$ | Hydrogen sulfide |
| KK | Kramers-Kronig |
| MT | Mass transport |
| $N_2$ | Nitrogen |
| $O_3$ | Ozone |
| OCV | Open circuit voltage |
| PA | Phosphoric acid |
| PBI | Polybenzimidazole |
| PC | Potential curve |
| PEEK | Poly ether ether ketone |
| PEM | Polymer electrolyte membrane |
| PSA | Pressure swing adsorption |
| Pt | Platinum |
| PTFE | Polytetrafluorethylene |
| RH | Relative humidity |
| $R_{HF}$ | High frequency resistance |

| | |
|---|---|
| $R_{LF}$ | Low frequency resistance |
| $R_M$ | Membrane resistance |
| $R_{tot}$ | Total resistance |

## References


[1] T.A. Aarhaug, O. Kjos, T. Bacquart, V. Valter, T. Optenhostert, Assessment of hydrogen quality dispensed for hydrogen refuelling stations in Europe, Int. J. Hydrogen Energy 46 (2021) 29501–29511, https://doi.org/10.1016/j.ijhydene.2020.11.163.

[2] M. Rhandi, M. Trégaro, F. Druart, J. Deseure, M. Chatenet, Electrochemical hydrogen compression and purification versus competing technologies: Part I. Pros and cons, Chin. J. Catal. 41 (2020) 756–769, https://doi.org/10.1016/S1872-2067(19)63404-2.

[3] S. Sircar, T.C. Golden, Purification of hydrogen by pressure swing adsorption, Separ. Sci. Technol. 35 (2000) 667–687, https://doi.org/10.1081/SS-100100183.

[4] M.D. Dolan, D.M. Viano, M.J. Langley, K.E. Lamb, Tubular vanadium membranes for hydrogen purification, J. Membr. Sci. 549 (2018) 306–311, https://doi.org/10.1016/j.memsci.2017.12.031.

[5] G. Sdanghi, G. Maranzana, A. Celzard, V. Fierro, Review of the current technologies and performances of hydrogen compression for stationary and automotive applications, Renew. Sustain. Energy Rev. 102 (2019) 150–170, https://doi.org/10.1016/j.rser.2018.11.028.

[6] S. Jiménez, J. Soler, R.X. Valenzuela, L. Daza, Assessment of the performance of a PEMFC in the presence of CO, J. Power Sources 151 (2005) 69–73, https://doi.org/10.1016/j.jpowsour.2005.02.049.

[7] C.L. Gardner, M. Ternan, Electrochemical separation of hydrogen from reformate using PEM fuel cell technology, J. Power Sources 171 (2007) 835–841, https://doi.org/10.1016/j.jpowsour.2007.06.020.

[8] R. Doucet, C.L. Gardner, M. Ternan, Separation of hydrogen from hydrogen/ethylene mixtures using PEM fuel cell technology, Int. J. Hydrogen Energy 34 (2009) 998–1007, https://doi.org/10.1016/j.ijhydene.2008.10.069.

[9] C. Jackson, L.F.J.M. Raymakers, M.J.J. Mulder, A.R.J. Kucernak, Poison mitigation strategies for the use of impure hydrogen in electrochemical hydrogen pumps and fuel cells, J. Power Sources 472 (2020), 228476, https://doi.org/10.1016/j.jpowsour.2020.228476.

[10] M.T. Nguyen, S.A. Grigoriev, A.A. Kalinnikov, A.A. Filippov, P. Millet, V.N. Fateev, Characterisation of a electrochemical hydrogen pump using electrochemical impedance spectroscopy, J. Appl. Electrochem. 41 (2011) 1033–1042, https://doi.org/10.1007/s10800-011-0341-9.

[11] K.A. Perry, G.A. Eisman, B.C. Benicewicz, Electrochemical hydrogen pumping using a high-temperature polybenzimidazole (PBI) membrane, J. Power Sources 177 (2008) 478–484, https://doi.org/10.1016/j.jpowsour.2007.11.059.

[12] F. Huang, A.T. Pingitore, B.C. Benicewicz, Electrochemical hydrogen separation from reformate using high-temperature polybenzimidazole (PBI) membranes: the role of chemistry, ACS Sustain. Chem. Eng. 8 (2020) 6234–6242, https://doi.org/10.1021/acssuschemeng.9b07037.

[13] F. Huang, A.T. Pingitore, B.C. Benicewicz, High polymer content m/p-Polybenzimidazole copolymer membranes for electrochemical hydrogen separation under differential pressures, J. Electrochem. Soc. 167 (2020), 063504, https://doi.org/10.1149/1945-7111/ab81a0.

[14] G. Venugopalan, D. Bhattacharya, E. Andrews, L. Briceno-Mena, J. Romagnoli, J. Flake, C.G. Arges, Electrochemical pumping for challenging hydrogen separations, ACS Energy Lett. 7 (2022) 1322–1329, https://doi.org/10.1021/acsenergylett.1c02853.

[15] M. Thomassen, E. Sheridan, J. Kvello, Electrochemical hydrogen separation and compression using polybenzimidazole (PBI) fuel cell technology, J. Nat. Gas Sci. Eng. 2 (2010) 229–234, https://doi.org/10.1016/j.jngse.2010.10.002.

[16] E. Ivers-Tiffée, A. Weber, Evaluation of electrochemical impedance spectra by the distribution of relaxation times, J. Ceram. Soc. Japan. 125 (2017) 193–201, https://doi.org/10.2109/jcersj2.16267.

[17] S. Dierickx, A. Weber, E. Ivers-Tiffée, How the distribution of relaxation times enhances complex equivalent circuit models for fuel cells, Electrochim, Acta 355 (2020), 136764, https://doi.org/10.1016/j.electacta.2020.136764.

[18] M. Schönleber, E. Ivers-Tiffée, Approximability of impedance spectra by RC elements and implications for impedance analysis, Electrochem. Commun. 58 (2015) 15–19, https://doi.org/10.1016/j.elecom.2015.05.018.

[19] T.H. Wan, M. Saccoccio, C. Chen, F. Ciucci, Influence of the discretization methods on the distribution of relaxation times deconvolution: implementing radial basis functions with DRTtools, Electrochim. Acta 184 (2015) 483–499, https://doi.org/10.1016/j.electacta.2015.09.097.

[20] M. Heinzmann, A. Weber, E. Ivers-Tiffée, Advanced impedance study of polymer electrolyte membrane single cells by means of distribution of relaxation times, J. Power Sources 402 (2018) 24–33, https://doi.org/10.1016/j.jpowsour.2018.09.004.

[21] N. Bevilacqua, M.A. Schmid, R. Zeis, Understanding the role of the anode on the polarization losses in high-temperature polymer electrolyte membrane fuel cells using the distribution of relaxation times analysis, J. Power Sources 471 (2020), 228469, https://doi.org/10.1016/j.jpowsour.2020.228469.

[22] A. Weiß, S. Schindler, S. Galbiati, M.A. Danzer, R. Zeis, Distribution of relaxation times analysis of high-temperature PEM fuel cell impedance spectra, Electrochim. Acta 230 (2017) 391–398, https://doi.org/10.1016/j.electacta.2017.02.011.

[23] J. Halter, N. Bevilacqua, R. Zeis, T.J. Schmidt, F.N. Büchi, The impact of the catalyst layer structure on phosphoric acid migration in HT-PEFC – an operando X-ray tomographic microscopy study, J. Electroanal. Chem. 859 (2020), 113832, https://doi.org/10.1016/j.jelechem.2020.113832.

[24] N. Bevilacqua, T. Asset, M.A. Schmid, H. Markötter, I. Manke, P. Atanassov, R. Zeis, Impact of catalyst layer morphology on the operation of high temperature PEM fuel cells, J. Power Sources Adv. 7 (2021), 100042, https://doi.org/10.1016/j.powera.2020.100042.

[25] J. Müller-Hülstede, T. Zierdt, H. Schmies, D. Schonvogel, Q. Meyer, C. Zhao, P. Wagner, M. Wark, Implementation of different Fe–N–C catalysts in high temperature proton exchange membrane fuel cells – effect of catalyst and catalyst layer on performance, J. Power Sources 537 (2022), 231529, https://doi.org/10.1016/j.jpowsour.2022.231529.

[26] A. Leonide, V. Sonn, A. Weber, E. Ivers-Tiffée, Evaluation and modeling of the cell resistance in anode-supported solid oxide fuel cells, J. Electrochem. Soc. 155 (2008) B36, https://doi.org/10.1149/1.2801372.

[27] A. Kromp, A. Leonide, A. Weber, E. Ivers-Tiffée, Electrochemical analysis of reformate-fuelled anode supported SOFC, J. Electrochem. Soc. 158 (2011) B980, https://doi.org/10.1149/1.3597177.

[28] H. Schichlein, A.C. Müller, M. Voigts, A. Krügel, E. Ivers-Tiffée, Deconvolution of electrochemical impedance spectra for the identification of electrode reaction mechanisms in solid oxide fuel cells, J. Appl. Electrochem. 32 (2002) 875–882, https://doi.org/10.1023/A:1020599525160.

[29] J. Illig, M. Ender, T. Chrobak, J.P. Schmidt, D. Klotz, E. Ivers-Tiffée, Separation of charge transfer and contact resistance in LiFePO 4 -cathodes by impedance modeling, J. Electrochem. Soc. 159 (2012) A952–A960, https://doi.org/10.1149/2.030207jes.

[30] J.P. Schmidt, P. Berg, M. Schönleber, A. Weber, E. Ivers-Tiffée, The distribution of relaxation times as basis for generalized time-domain models for Li-ion batteries, J. Power Sources 221 (2013) 70–77, https://doi.org/10.1016/j.jpowsour.2012.07.100.

[31] M. Schilling, M. Braig, K. Köble, R. Zeis, Investigating the V(IV)/V(V) electrode reaction in a vanadium redox flow battery – a distribution of relaxation times analysis, Electrochim. Acta 430 (2022), https://doi.org/10.1016/j.electacta.2022.141058.

[32] J. Schneider, T. Tichter, P. Khadke, R. Zeis, C. Roth, Deconvolution of electrochemical impedance data for the monitoring of electrode degradation in VRFB, Electrochim. Acta 336 (2020), 135510, https://doi.org/10.1016/j.electacta.2019.135510.

[33] A. Huth, B. Schaar, T. Oekermann, A “proton pump” concept for the investigation of proton transport and anode kinetics in proton exchange membrane fuel cells, Electrochim. Acta 54 (2009) 2774–2780, https://doi.org/10.1016/j.electacta.2008.11.010.

[34] S.J. Kim, B.S. Lee, S.H. Ahn, J.Y. Han, H.Y. Park, S.H. Kim, S.J. Yoo, H.J. Kim, E. Cho, D. Henkensmeier, S.W. Nam, T.H. Lim, S.K. Kim, W. Huh, J.H. Jang, Characterizations of polybenzimidazole based electrochemical hydrogen pumps with various Pt loadings for H2/CO2 gas separation, Int. J. Hydrogen Energy 38 (2013) 14816–14823, https://doi.org/10.1016/j.ijhydene.2013.08.142.

[35] G. Venugopalan, D. Bhattacharya, S. Kole, C. Ysidron, P.P. Angelopoulou, G. Sakellariou, C.G. Arges, Correlating high temperature thin film ionomer electrode binder properties to hydrogen pump polarization, Mater. Adv. 2 (2021) 4228–4234, https://doi.org/10.1039/d1ma00208b.

[36] M. Schönleber, D. Klotz, E. Ivers-Tiffée, A method for improving the robustness of linear kramers-kronig validity tests, Electrochim. Acta 131 (2014) 20–27, https://doi.org/10.1016/j.electacta.2014.01.034.

[37] C.A. Schiller, R. Kaus, On-line error determination and processing for electrochemical impedance spectroscopy measurement data based on weighted harmonics autocorrelation, Bulg. Chem. Commun. 41 (2009) 192–198.

[38] M. Hahn, S. Schindler, L.C. Triebs, M.A. Danzer, Optimized process parameters for a reproducible distribution of relaxation times analysis of electrochemical systems, Batteries 5 (2019), https://doi.org/10.3390/batteries5020043.

[39] S.J. Andreasen, J.R. Vang, S.K. Kær, High temperature PEM fuel cell performance characterisation with CO and CO2 using electrochemical impedance spectroscopy, Int. J. Hydrogen Energy 36 (2011) 9815–9830, https://doi.org/10.1016/j.ijhydene.2011.04.076.

[40] J.H. Perry, D.W. Green, M.Z. Southard, Perry’s Chemical Engineers’ Handbook, ninth ed., McGraw-Hill Education, New York, 2019.

[41] R.F. Mann, J.C. Amphlett, B.A. Peppley, C.P. Thurgood, Application of Butler-Volmer equations in the modelling of activation polarization for PEM fuel cells, J. Power Sources 161 (2006) 775–781, https://doi.org/10.1016/j.jpowsour.2006.05.026.

[42] A.D. Modestov, M.R. Tarasevich, V.Y. Filimonov, E.S. Davydova, CO tolerance and CO oxidation at Pt and Pt-Ru anode catalysts in fuel cell with polybenzimidazole-H3PO4 membrane, Electrochim. Acta 55 (2010) 6073–6080, https://doi.org/10.1016/j.electacta.2010.05.068.

[43] S.J. Kim, H.Y. Park, S.H. Ahn, B. seok Lee, H.J. Kim, E.A. Cho, D. Henkensmeier, S. W. Nam, S.H. Kim, S.J. Yoo, J.H. Jang, Highly active and CO2 tolerant Ir nanocatalysts for H2/CO2 separation in electrochemical hydrogen pumps, Appl. Catal. B Environ. 158–159 (2014) 348–354, https://doi.org/10.1016/j.apcatb.2014.04.016.

[44] A. Kulikovsky, A model–based analysis of PEM fuel cell distribution of relaxation times, Electrochim. Acta 429 (2022), 141046, https://doi.org/10.1016/j.electacta.2022.141046.

[45] S. Martin, Q. Li, J.O. Jensen, Lowering the platinum loading of high temperature polymer electrolyte membrane fuel cells with acid doped polybenzimidazole membranes, J. Power Sources 293 (2015) 51–56, https://doi.org/10.1016/j.jpowsour.2015.05.031.

[46] S.H. Eberhardt, F. Marone, M. Stampanoni, F.N. Büchi, T.J. Schmidt, Operando X-ray tomographic microscopy imaging of HT-PEFC: a comparative study of phosphoric acid electrolyte migration, J. Electrochem. Soc. 163 (2016) F842–F847, https://doi.org/10.1149/2.0801608jes.
[47] S.H. Eberhardt, M. Toulec, F. Marone, M. Stampanoni, F.N. Büchi, T.J. Schmidt, Dynamic operation of HT-PEFC: in-operando imaging of phosphoric acid profiles and (Re)distribution, J. Electrochem. Soc. 162 (2015) F310–F316, https://doi.org/10.1149/2.0751503jes.
[48] H. Becker, L.N. Cleemann, D. Aili, J.O. Jensen, Q. Li, Probing phosphoric acid redistribution and anion migration in polybenzimidazole membranes, Electrochem. Commun. 82 (2017) 21–24, https://doi.org/10.1016/j.elecom.2017.07.005.
[49] M. Ehsasi, M. Matloch, O. Frank, J.H. Block, K. Christmann, F.S. Rys, W. Hirschwald, Steady and nonsteady rates of reaction in a heterogeneously catalyzed reaction: oxidation of CO on platinum, experiments and simulations, J. Chem. Phys. 91 (1989) 4949–4960, https://doi.org/10.1063/1.456736.
[50] Y. Oono, T. Fukuda, A. Sounai, M. Hori, Influence of operating temperature on cell performance and endurance of high temperature proton exchange membrane fuel cells, J. Power Sources 195 (2010) 1007–1014, https://doi.org/10.1016/j.jpowsour.2009.08.097.
[51] S. Yu, L. Xiao, B.C. Benicewicz, Durability studies of PBI-based high temperature PEMFCs, Fuel Cell. 8 (2008) 165–174, https://doi.org/10.1002/fuce.200800024.
[52] C. Korte, Phosphoric acid, an electrolyte for fuel cells - temperature and composition dependence of vapor pressure and proton conductivity, Fuel Cell Sci. Eng. Mater. Process. Syst. Technol. 1 (2012) 335–359, https://doi.org/10.1002/9783527650248.ch12.
[53] N. Zamel, N.G.C. Astrath, X. Li, J. Shen, J. Zhou, F.B.G. Astrath, H. Wang, Z.S. Liu, Experimental measurements of effective diffusion coefficient of oxygen-nitrogen mixture in PEM fuel cell diffusion media, Chem. Eng. Sci. 65 (2010) 931–937, https://doi.org/10.1016/j.ces.2009.09.044.
[54] J.P. Melchior, K.D. Kreuer, J. Maier, Proton conduction mechanisms in the phosphoric acid-water system (H4P2O7-H3PO4·2H2O): a 1H, 31P and 17O PFG-NMR and conductivity study, Phys. Chem. Chem. Phys. 19 (2017) 587–600, https://doi.org/10.1039/c6cp04855b.
[55] K. Klinedinst, J.A.S. Bett, J. Macdonald, P. Stonehart, Oxygen solubility and diffusivity in hot concentrated H3PO4, J. Electroanal. Chem. 57 (1974) 281–289, https://doi.org/10.1016/S0022-0728(74)80053-7.
[56] F. Gan, D.T. Chin, Determination of diffusivity and solubility of oxygen in phosphoric acid using a transit time on a rotating ring-disc electrode, J. Appl. Electrochem. 23 (1993) 452–455, https://doi.org/10.1007/BF00707621.
[57] K.E. Gubbins, R.D. Walker, The solubility and diffusivity of oxygen in electrolytic solutions, J. Electrochem. Soc. 112 (1965) 469, https://doi.org/10.1149/1.2423575.
[58] F. Mack, T. Morawietz, R. Hiesgen, D. Kramer, V. Gogel, R. Zeis, Influence of the polytetrafluoroethylene content on the performance of high-temperature polymer electrolyte membrane fuel cell electrodes, Int. J. Hydrogen Energy 41 (2016) 7475–7483, https://doi.org/10.1016/j.ijhydene.2016.02.156.
[59] J.P. Melchior, G. Majer, K.D. Kreuer, Why do proton conducting polybenzimidazole phosphoric acid membranes perform well in high-temperature PEM fuel cells? Phys. Chem. Chem. Phys. 19 (2017) 601–612, https://doi.org/10.1039/c6cp05331a.
[60] J. Durst, C. Simon, F. Hasché, H.A. Gasteiger, Hydrogen oxidation and evolution reaction kinetics on carbon supported Pt, Ir, Rh, and Pd electrocatalysts in acidic media, J. Electrochem. Soc. 162 (2015) F190–F203, https://doi.org/10.1149/2.0981501jes.